Multi-Satellite Comparisons of the Radiation Belt Response to the GEM magnetic storms

K. L. McAdams, G. D. Reeves, R. H. W. Friedel, and T. E. Cayton

Los Alamos National Laboratory, Los Alamos, New Mexico

Short title: GEM STORM COMPARISONS

Abstract. We present a compilation of observations of relativistic radiation belt electrons during the four GEM storms from instruments on 10 separate spacecraft. While these four magnetic storms have very different solar wind and magnetospheric conditions, there are several characteristics of the relativistic electron response which are applicable to all four storms. We find that although the evolution of the spectral shape of the electrons at a specific L-shell does not vary from storm to storm, the evolution is very different at $L = 4.2$ and $L = 6.6$. Calculations of the phase space density (PSD) show that the evolution of the PSD depends on both radial position and the value of the first adiabatic invariant. The evolution of the greater than 1 MeV electron flux at $L = 4.2$ and $L = 6.6$ for the four storms is consistent with the findings of *Reeves et al.* [1998c]. The flux at $L = 4.2$ peak quickly after the storm (12 hours), while the fluxes at geosynchronous altitudes take several days to rise. We suggest that the common characteristics identified in the four storms that are the subject of this paper can provide a useful basis for comparisons with other storms and for development of a more complete theoretical description of relativistic electron events in general.

1. Introduction

The population of relativistic electrons in the Earth's outer radiation belt ($2 < L < 7$) varies dramatically with magnetic activity. As we increase our reliance on satellite technology, the response of the radiation belt electrons to magnetospheric conditions is of more than academic interest because elevated relativistic electron fluxes can interfere with satellite operations. We have combined several satellite data sets to investigate the response of the radiation belts to four different magnetic storms. We seek to identify the general characteristics of the relativistic electron enhancements in order to place more precise observational constraints on models of radiation belt electron acceleration during magnetic storms. This study also serves to further illuminate how data from many satellites can be combined to increase the coverage of measurements of the radiation belts [*Friedel et al.*, 1999; *Reeves et al.*, 1998b].

Although the relationship between relativistic electron fluxes and magnetic storms has been known for many years [*Paulikas and Blake*, 1979], it is not clear by what mechanism magnetic storms accelerate the relativistic electron population. Several studies have examined the temporal development at different L-shells of individual storms [*Reeves et al.*, 1998c, a; *Selesnick and Blake*, 2000], but have not compared the development of several storms. Using a multi-satellite data set we compare the evolution of four different storms as a function of time, L-shell, energy and adiabatic invariants. Finding a set of common characteristics for relativistic electron events is a crucial step in answering some of the outstanding questions regarding their acceleration and transport.

The location of the peak in the phase space density (PSD) of the electrons is still a point of debate and indeed may vary from storm to storm [*Selesnick and Blake*, 2000; *Green et al.*, 1999; *Brautigam and Albert*, 2000]. Few observations of the peak PSD have been made, primarily because phase space density measurements using adiabatic coordinates are difficult to calculate, as they require good energy and pitch angle resolution as well as reliable magnetic field measurements and models. Unfortunately, most magnetic field models are not valid during storm-time disturbances – the precise time interval in which electron enhancements occur. Another piece of the puzzle which is key to several acceleration mechanisms [*Li et al.*, 1999], is whether there is a population of "seed" electrons in the outer magnetosphere, where that population might be located, and what its source may be.

There are several competing and sometimes overlapping theories to explain the observed increase of the relativistic electron fluxes which occurs in magnetic storms. There is evidence that, when there is a large shock compression of the magnetosphere, the generation of a large induction electric field can rapidly accelerate an existing electron seed population which subsequently moves to lower L-shells to preserve the third adiabatic invariant [*Li et al.*, 1998]. While this mechanism is well-accepted for a certain class of events, in most storms there is no large compressional shock and other mechanisms must be invoked. *Nishida* [1976] and *Fujimoto and Nishida* [1990] proposed a magnetic pumping/recirculation model, in which radial and pitch angle diffusion combine to slowly accelerate electrons through successive cycles, moving particles in to lower L-shells and back out to higher ones. *Liu et al.* [1999] modified this theory

by incorporating ULF waves rather than pitch angle diffusion by plasmaspheric hiss to scatter the electrons in order to speed up the cycle time, resulting in a time scale of electron heating consistent with observations of the electron response to storms. Others have incorporated ULF wave interactions in several ways to directly heat the electrons to high energies (i.e., *Hudson et al.* [1999]; *Elkington et al.* [1999]). Whistler mode interactions with the electrons near the plasmapause are also considered by *Abel and Thorne* [1998a, b] .

The geospace Environmental Modelling (GEM) program is an ogoing effort sponsored by the US National Science Foundation. GEM is organized around scientific campaigns. One of these is the Inner Magnetosphere/Storms campaign[1].

In order to provide a common basis for observations, theory and modelling the GEM community has identified three magnetic storms for in-depth study and comparison. These storms are May 15, 1997; September 25, 1998; and October 20, 1998; we have included January 10, 1997, as a well studied example of a magnetic storm accompanied by a compressional shock.

2. Data Synthesis

Data from a single spacecraft has the well known drawback that single point measurements cannot differentiate spatial and temporal variations. Synthesizing data from many spacecraft into a single data set, providing both space and time coverage,

[1]http://leadbelly.lanl.gov/GEM_Storms

allows a more complete view of radiation belt dynamics. Instruments on different satellites vary from high energy and pitch-angle resolution detectors designed to explore the radiation belts, to dosimeters built primarily to understand the radiation dose at the satellite. By combining data sets from various instruments, we can often "bootstrap" the data from a low-resolution instrument by using pitch angle or magnetic field measurements from nearby spacecraft to make informed assumptions applicable at other satellites.

For this study, we have included data from ten satellites, each with electron instruments that detect electrons greater than 1 MeV although the additional instruments on each payload vary widely. We use data from POLAR [*Blake et al.*, 1995], SAMPEX [*Baker et al.*, 1993], HEO [*Blake et al.*, 1997], GPS (NS24 and NS33) [*Feldman et al.*, 1985], GOES 8 and 9 [*Space-Systems-Loral*, 1996], and the Los Alamos National Laboratory (LANL) geosynchronous satellites 1994-084, 1991-080, and 1990-095 [*Meier et al.*, 1996]. All of the satellites have some drawbacks due to energy resolution, pitch angle coverage or orbital characteristics. Details of the individual satellites are given in Table 1 and the Appendix as well as in the various references. Unless specifically noted, all flux values quoted assume isotropic equatorial pitch angle distributions and integral energy ranges.

Table 1.

3. GEM Storms

Figure 1.

The GEM magnetic storms were chosen to represent a variety of storm-time conditions in the magnetosphere. Figure 1 shows the magnetospheric and solar wind

conditions throughout the four storms. The first panel of each stack shows the Dst index (courtesy of WDC-C2, Kyoto), the next panel shows the Kp index (courtesy of WDC-A, Boulder), and the lower three panels show solar wind conditions observed by the WIND spacecraft including IMF B_z [*Lepping et al.*, 1995], solar wind velocity (v_{sw}), and the solar wind ion density (n) [*Ogilvie et al.*, 1995] (data provided through the CDAWeb data server, http://cdaweb.gsfc.nasa.gov). **Table 2.**

Table 2 summarizes the solar wind and magnetospheric conditions and the relativistic electron response for the four storms which are discussed in more detail below.

The global radiation belt response to these storm conditions is depicted in Plate 1 where results of the data synthesis are shown. Combining ten single-satellite data sets into a coherent picture of the radiation belts requires careful data manipulation. Differences in the energy and pitch angle ranges must be accounted for as well as any latitudinal variation. Compounding this problem, we often do not know the pitch angle distribution at each satellite, nor do we have detailed spectral information from each satellite. Therefore, we have made several–admittedly simplistic–assumptions: **Plate 1.**

1. The pitch angle distribution is isotropic throughout the evolution of the storm. This is almost certainly not valid for some of the time, as *West et al.* [1973] have shown that the distribution tends to form butterfly or pancake distributions. However, isotropy is a commonly invoked assumption and is likely to be accurate immediately after the storm [*Friedel and Korth*, 1997].

2. The spectral shape does not change drastically at energies greater than 1 MeV. This

allows us to compare flux from a 1 MeV channel to flux from a 2.0 MeV channel and use a constant normalization factor throughout the storm. This assumption is fairly good at lower L-shells, as we show later in the paper (see Section 4.2).

3. L-shells are calculated using the Olson Pfitzer [1977] static magnetic field model and therefore do not accommodate any storm-time changes is the true magnetic field.

By simultaneously including data from satellites at the same nominal L-shell but different magnetic local times (MLT), we can show either local time differences in the flux evolution or, as is done here, average over these differences and show a more general picture of the global electron flux evolution. The techniques we use to create a multi-satellite flux data set are applied only to observations of the greater than 1.5 MeV electron fluxes and not to any spectral data sets presented here. These maps of the relativistic electron fluxes as a function of L and time are created by binning the data sets by L and time and ignoring any local time variation in the fluxes.

3.1. January 1997

If only the response of the ring current is considered, the January 10, 1997, (January 97) magnetic storm was a fairly moderate storm [*Gonzalez et al.*, 1994]. The minimum Dst reached only a fairly modest -78 nT. However, less than a day after the beginning of the storm, the magnetic cloud that caused the storm created a compressional shock which pushed the magnetopause deep into the inner magnetosphere. The solar wind velocity was close to 600 km/s and the density pulse was near 200 cm^{-3} (see Figure 1a). This resulted in a rapid increase in the relativistic electron fluxes over a broad range of

L-shells. After the initial flux increase, the particle flux at high L values (near $L = 6.6$) decreased quickly and then gradually peaked a few days later as is typical for > 1.5 MeV electrons at $L = 6.6$ (Plate 1a). The initial flux increase at lower L-values ($L = 4.5$) persisted throughout the duration of the recovery phase of the storm [*Reeves et al.*, 1998c]. *Li et al.* [1998] determined that a pre-existing source of particles was energized by the pressure pulse which pushed the electrons into regions of stronger magnetic field (assuming the first adiabatic invariant was conserved, the particles must gain energy as a result of the transport).

3.2. May 1997

The May 15, 1997, storm (May 97) was a much larger storm and was a fairly "typical" storm in terms of its simple Dst profile and electron response. However, a small magnetic disturbance at the beginning of the month may have contributed to high flux levels observed prior to the storm onset. In this storm, the Dst minimum of -115 nT coincided with the ramping up of the solar wind velocity (Figure 1b). The solar wind velocity continued to increase throughout the main phase of the storm to a maximum of over 500 km/s.

The response of the relativistic electrons was much stronger than in January 97 as is shown in Plate 1b. The fluxes at low L quickly rise to, and then persist at levels much higher than the January 97 storm (see Table 2). At higher L-shells the relativistic electron fluxes take several days to peak at slightly higher flux levels than the January storm. *Baker et al.* [1998] concluded that ULF waves were probably important in the

electron acceleration for this event.

3.3. September 1998

The largest and most complex storm in this study is September 25, 1998 (September 98). This storm is a compound event with a large storm (Dst minimum = -233 nT) on September 25 (Day 268)and then a secondary Dst dip of -69 nT on October 1 (Day 274) (Figure 1c). In this event, the solar wind velocity peaks sharply at a maximum of 901 km/s. A second peak in the solar wind velocity follows the October 1 Dst drop. Before the storm occurs there is a pre-existing high relativistic-electron flux at low L (near $L = 3.5$). Plate 1c shows the structure in the Dst profile reflected in the electron fluxes as they increase after the first main phase and then decrease again after the second onset occurs. The electron fluxes recover after the second decrease, but do not reach the previous levels of intensity.

3.4. October 1998

The October 20, 1998 (October 98) storm has an interesting solar wind profile. At the time of the Dst minimum (-139 nT), the IMF magnitude increases sharply and the solar wind density peaks at 68 cm^{-3}, much higher than either May 97 or September 98 (Figure 1d). The solar wind velocity, however, does not peak at the Dst minimum, but continues to rise for a little over two days to a maximum of 693 km/s. Kp values peak at 6^{+} coincident with the Dst minimum and then continue to remain active for the next ten days whereas the September 98 storm had a sharp peak in Kp that tapered off more

quickly. Diffusion coefficients are often parameterized by Kp values in diffusion models such as the Salammbô codes [*Bourdarie et al.*, 1997].

The electron response is different than that of the other storms (See Plate 1d). At $L = 6.6$ the peak in relativistic electron flux is higher than the $L = 6.6$ peak for the September 98 storm even though the September 98 storm produced much higher flux levels at lower L values (i.e. L near 4). The ratio of fluxes at $L = 4.25$ to fluxes at $L = 6.6$ is 57 for September 98 and 15 for October 98. The rise in flux intensities at lower L shells was also more gradual than in the other 3 storms in this study. During the other three storms, the $L = 4.2$ fluxes rise quickly and then plateau, while in October 98 they rise with a more quasi-parabolic temporal profile. This may be attributed in part to the outward movement of the peak in the radial flux profile during the October 98 storm. The peak moves from $L \sim 4$ at day 294 to $L \sim 5$ at day 296. During the other storms, the peak was more or less static although in May 97 the peak moved slightly inward until day 144.

4. Evolution of the Storms at Different L-shells

In all four of the storms, the evolution of the relativistic electron population varies with L-shell. We examined the flux evolution at several L-shells to determine the relativistic electron acceleration at different radial positions. We present the temporal profiles of intensity, spectral shape and phase space density at $L = 4.2$ and $L = 6.6$.

4.1. Flux Intensities

Reeves et al. [1998c] showed that for the January 97 storm the time profiles of the fluxes at $L = 4.25$ and $L = 6.6$ were very different: the $L = 4.25$ fluxes peaked sooner than the $L = 6.6$ fluxes. Plate 2 shows the relativistic electron fluxes at $L = 4.25 \pm 0.125$ and $L = 6.6 \pm 0.125$ for the four storms. **Plate 2.**

These fluxes are taken from the synthesis data set and the individual satellite fluxes are color-coded. The spread in fluxes at a given L-shell (particularly noticeable at $L = 6.6$) is likely due to latitudinal effects and differences in the energy ranges of individual satellites in addition to the limitations of the magnetic field model in calculating the L-shell values. January 97 (Plate 2a) and September 98 (Plate 2c) are similar to May 97 in their temporal profiles of the electron flux and comments made about the May 97 storm in reference to this aspect can be applied to them. In Plate 2b, the flux profile at $L = 4.25$ is different from the profile at $L = 6.6$. At $L = 4.25$, the fluxes rise quickly and then plateau, while at $L = 6.6$ the fluxes slowly rise in a quasi-parabolic shape to peak after a few days. This profile is consistent with the findings of *Reeves et al.* [1998c]. The behavior of the electrons during the October 98 storm is different from the other three storms at $L = 4.25$ (Plate 2d). The profile at $L = 4.25$ shows a more gradual peak in the fluxes rather than a sharp rise which plateaus after a few hours. As noted earlier, this may be related to the apparent outward movement of the radial peak in the electron flux.

It is useful here to compare the electron response of October 98 to both May 97

and September 98. May 97 has lower flux levels at both $L = 4.25$ and $L = 6.6$ than October 98 although the two storms have comparable Dst minimums. The elevated October 98 fluxes compared to May 97 may be due to the larger solar wind velocity and the extended period of active Kp during the October 98 storm. Somewhat predictably, the stronger Dst minimum of the September 98 storm leads to stronger flux levels at $L = 4.25$ than during the October 98 storm. However, electron fluxes at $L = 6.6$ are stronger during October 98 than September 98. During October 98, the solar wind velocity continues to climb as the storm progresses, rather than peaking at the same time as the Dst minimum as in September 98. The Kp profile for September 98 shows a short period of intense activity which dies away quickly after a few days, while the Kp index during October 98 shows activity $\gtrsim 2$ for ten days.

These different responses at October 98 may be related to the differences in the magnetospheric conditions present during the October storm. Rather than peaking sharply at the time of the Dst minimum, the solar wind velocity continued to ramp up during the main phase of the October 98 storm. Although one might expect that the continued high solar wind velocity was driving a strong convection electric field during the October 98 event, the maximum polar cap index (PCI, courtesy of WDC-A in Boulder) during September 98 was twice as strong as in October 98 indicating a stronger convection field during September 98. The PCI continued to be active for several days at near equal levels for both storms after the peak. Kp values also remained elevated for several days after the initial burst of activity corresponding to the Dst drop. The Kp index continues to show disturbed conditions with fluctuations up to 4.0 for 5-6 days in

October 98 while for September 98 the disturbed Kp conditions lasted only two days. There are indications that the position of the plasmapause and the diffusion coefficients (both of which can be parameterized by Kp index) are important in determining the diffusive evolution of the "original" spectra. Both of these may have contributed to a continued acceleration of the electrons at $L = 4.25$ and may have played a part in increasing the geosynchronous electron flux to levels higher than during the September 98 storm.

4.2. Spectral Shape

We investigate whether the rise of the relativistic fluxes is due to a change in the spectral shape at high energies. To answer this question, we calculate the energy spectra from electron fluxes at a range of energies from near the equator at $L = 4.25$ (GPS NS33), and $L = 6.6$ (LANL). We take only near-equatorial fluxes so that changes in the spectra due to latitudinal variations can be ignored safely. The energy range for GPS NS33 is 0.275–2.2 MeV and for the LANL satellites we use energies in the range 0.200–3.2 MeV. We fit the flux energy spectra to an exponential: $j(E) = C \exp(-E/E_o)$ where j is the energy flux and E is energy. (We tried other functional forms, but found that the exponential fit provided the best fit.)

Plate 3.

Plate 3 shows the evolution of C ("density") and E_o ("temperature") at $L = 4.25$ (GPS) and $L = 6.6$ (LANL). In all four storms there is a fast rise in the C parameter at the main phase of the storm and then a slow, steady decrease at $L = 4.25$. There is more variation in the behavior of C at $L = 6.6$, but it follows the pattern of a quick increase

followed by a decrease of some sort. At geosynchronous altitudes, all four storms show a gradual rise of E_o, or hardening of the spectra, and then a decline after 7-10 days when the storm is over. (Note that only January 97 and October 98 have good spectral information for the complete storm.) At $L = 4.25$ there is a small drop in E_o at the Dst minimum and then a steady rise corresponding to the recovery phase which continues to rise throughout the depicted interval. The rise in E_o is noticeably steeper at $L = 4.25$ than at $L = 6.6$. The September 98 storm is noticeable in the dip of E_o at both L shells (Plate 3c) corresponding to the second episode of geomagnetic activity. It is notable that for all four storms the value of E_o at $L = 4.2$ is near 400 during the Dst minimum even though the pre-storm starting points are quite different.

The evolution of the high energy electron spectrum during the storm is similar across all four storms regardless of magnetospheric conditions. This general response can be used to understand the basic physics of the storm-time response of the electrons for most (if not all) storms, hence we offer a physical interpretation of the spectral observations. The response at $L = 4.25$ suggests that during the storm main phase the high energy particles are lost quickly as they move to higher L-shells to conserve their adiabatic invariants (the so-called Dst effect) and the spectra softens at the same time that the "density" (C) of the population increases. As the storm progresses, the low energy particles are lost at a higher rate and the spectra slowly hardens without noticeable heating of the high energy tail. The losses can be inferred from the continuing decrease in C as the storm recovers. At geosynchronous altitudes ($L = 6.6$), the high energy particles are not lost at the Dst minimum and recovery, indeed, for all four

storms, E_o increases during the recovery and C increases for January 97 and remains flat for September 98 and October 98, indicating heating of the high energy electron tail or of an unlikely inflow of high energy particles without a corresponding low energy population. (For May 97, this does not appear to be the case as C decreases throughout the recovery at $L = 6.6$.) As the January 97 and October 98 storms progress, C continues to rise until it peaks about 2 days after the initial storm onsets. For the storms where there is enough spectral information to determine a peak in E_o, the peak occurs approximately 5-7 days after storm onset. For May 97 the peak in E_o cannot be determined as the spectral fit quality is low for the end of the storm. For January 97, October 98 and possibly September 98, the hardening of the spectra near geosynchronous orbit may be due to heating of the high energy tail, rather than losses of the lower energy electrons.

4.3. Phase Space Density

In locating the source of the electron acceleration, it is useful to remove the adiabatic effects from the flux observations so that the non-adiabatic variations are identifiable. One way to do this is to look at the phase space density (PSD) in a coordinate system consisting of the three adiabatic invariants. Calculating the PSD in adiabatic coordinates from the energy fluxes allows us to follow the motion of fluxes with constant adiabatic invariants. If the adiabatic invariants are conserved, than the radial PSD profile should not vary with time. The three adiabatic invariants of trapped particle motion are μ, J, and Φ which are associated with gyromotion, bounce motion

along the field line and the drift motion around the Earth, respectively. The first invariant is

$$\mu = \frac{p^2}{2mB_m} \tag{1}$$

where p is the momentum, m is the electron rest mass, and B_m is the magnetic field at the electron mirror point. The second invariant is defined by

$$J = \oint p_{||} ds \tag{2}$$

where $p_{||}$ is the parallel component of the momentum and ds is along the field line. The third invariant (Φ) can be replaced with the generalized L^* shell:

$$L^* = \frac{2\pi k_o}{a\Phi} \tag{3}$$

where Φ is the magnetic flux enclosed by an electron drift orbit, k_o is the Earth's dipole magnetic moment, and a is the Earth's radius [*Roederer*, 1970; *Schulz and Lanzerotti*, 1973]. We will use the simpler McIlwain L [*McIlwain*, 1966] which is calculated for the a single field line integral rather than the entire drift shell. By making this substitution, we ignore any Dst effect and any temporal changes in the magnetic field.

As mentioned earlier, a proper calculation of PSD requires both pitch-angle information and a precise knowledge of the magnetic field structure. We have neither. However, we can restrict the data sets to locations near the magnetic equator and assume the pitch-angle distribution is isotropic, or at least constant throughout the

storm. This allows us to treat the fluxes as if their second adiabatic invariant (J) were strictly zero. We treat the magnetic field as if it were accurately determined by the static Olson-Pfitzer field model [*Olson and Pfitzer*, 1977] and assume that the third invariant L^* is proportional to L-shell. By assuming that the particles are equatorially mirroring ($W_\perp = E$), we can assume that the first invariant is given by

$$\mu = \frac{E(1 + E/2E_r)}{B} \tag{4}$$

where E is the energy of the particle, E_r is the rest energy of the particle (0.511 MeV for an electron), and B is the magnetic field at the equator.

Thus, using the same spectra calculated above and by assuming that μ is defined by equation 4, $J = 0$ and $L^* \propto L$ we can have an estimate of the relativistic PSD at the equator such that

$$f(\mu, J, L^* \sim L) \propto \frac{j(E, \alpha, L)}{E(1 + E/2E_r)} \tag{5}$$

where f is the PSD, j is the particle flux, and E is the energy of the particles. Now we can compare the PSD at different values of μ for each L-shell above. **Plate 4.**

The response of the electrons if one looks at the phase space density is similar for all of the four storms particularly at $L = 4.25$. Plates 4 and 5 show the PSD at 4.25 (GPS), and 6.6 (LANL) for different values of μ. The range of μ corresponds to an energy range of 100 keV to 1.4 MeV at $L = 6.6$ and an energy range of 320 keV to 3.1 MeV at $L = 4.25$. At $L = 4.25$, after the initial increase at the Dst recovery, the PSD increases **Plate 5.**

with time at values of μ above some threshold value and decreases with time at values of constant μ less than the threshold. That threshold is near $\mu = 1000$ MeV/nT for January 97 (Plate 4a) and $\mu \sim 1000$ MeV/nT for May 97 (Plate 4b). For September 98 (Plate 5a), the transition appears to occur at lower values of $500 < \mu < 1000$ MeV/nT and for October 98 the transition is even lower at $\mu = 500$ MeV/nT (Fig 5b). At $L = 6.6$ all four storms have a similar quasi-parabolic shape throughout the storm at higher μ values (relativistic energies) while at lower μ values (corresponding to energies typical of substorm injections) the response is quite different from storm to storm. As with the energy fluxes, at $L = 6.6$ the PSD at higher μ values peaks after a few days. The profiles of the PSD values at different L-shells are different for higher μ which implies that the population is not simply diffusing inward, however, at lower values of μ, the PSD profiles are quite similar at the different L-shells. If the electrons were diffusing in from a distant source population, one would expect that the profiles would be similar even if they were offset by a time delay. However, the profiles shown here imply that there is an additional source of acceleration for the higher μ particles, other than simple radial diffusion.

Although we examine the PSD at only two L-shells, we can discuss the radial gradient between $L = 4.2$ and $L = 6.6$ bearing in mind we cannot identify the peak in PSD with only two measurements. For all four storms, the slope of the radial gradient decreases with increasing μ, although for all values of μ shown here, the gradient is positive (PSD increases with L-shell). All four storms show that the gradient decreases during the storm recovery, particularly at high μ values. This is consistent with the

findings of *Brautigam and Albert* [2000].

5. Discussion

We have examined the relativistic electron response to four different storms, including the three GEM storms (May 97, September 98,and October 98) and January 97. Although these four storms have differing solar wind and ring current conditions, there are a few traits in the electron response that are common to all four storms.

The evolution of the spectral shape of the electrons above 200 keV is different at $L = 4.25$ and $L = 6.6$, although it does not vary from storm to storm. We believe that the difference in the spectral shape may be because the hardening of the spectra at $L = 4.25$ is due to a preferential loss of the low energy electrons while the spectral hardening at $L = 6.6$ is due to an actual heating of the high energy tail rather than a loss of the low energy electrons.

Examining the phase space density evolution for several values of μ at $L = 6.6$ and $L = 4.25$ we found that the behavior is consistent for the four storms we studied. The PSD profiles are different at the two L-shells at high μ values. This implies that the energization in not due to diffusion alone, although it is likely that diffusion occurs along with one or more other energization processes. We found that at low μ values the PSD peaks first at $L = 4.25$ while at high μ values PSD peaks first at $L = 6.6$. Although the radial gradient in PSD is always positive, the magnitude of the slope decreases with increasing μ.

We found that the evolution of the 1.5 MeV fluxes at $L = 4.25$ and $L = 6.6$ was

similar for the January 97, May 97 and September 98 storms while October 98 seemed to have a different temporal profile. For the first three storms, the flux profiles were different at the different L values, but for October 98 the profiles were more similar. For all four storms, at $L = 6.6$ the profiles are quasi-parabolic in time. For the first three storms the profile at $L = 4.25$ is more plateau-like with a fast rise followed by steady flux levels. October 98 is unique among this study in that the $L = 4.25$ flux profile is more similar to that at $L = 6.6$ and is more quasi-parabolic than plateau-like. We attribute this difference in the October 98 flux response to the differences in the solar wind profiles and Kp values. We believe that the continued increase of the solar wind velocity may have contributed to continued acceleration of the electrons at $L = 4.25$. The continuing high levels of Kp disturbance may also have contributed to the continuing acceleration of these electrons.

We have found several similarities between the four storms which will help to constrain the theoretical explanations for the acceleration of the relativistic electrons in the radiation belt. Any mechanism to explain the electron acceleration will also have to explain the differences in the electron response to the October 98 storm conditions and the May 97 PSD profiles.

Acknowledgments.

We thank R. D. Belian, R. A. Christensen, and M. M. Meier for providing the LANL satellite data, S. Kulkarni and B. Blake for the SAMPEX data, R. Selesnick for the POLAR CEPPAD/HIST data, W. Feldman for the GPS data, and J. Fennell for the HEO data. This

work was supported by grants from NASA's International Solar Terrestrial Physics (ISTP) Program and from the US Department of Energy Office of Basic Energy Science (OBES).

Appendix: Synthesis Techniques

Combining data from ten satellites with different instruments requires some careful data manipulation. We build on work done by *Friedel et al.* [1999] in synthesizing many satellite data in order study the January 97 storm evolution at different local time and L-shell. The satellite instrumentation used in the current study is described briefly here. The POLAR satellite [*Blake et al.*, 1995] has the most complete instrument package in this set of satellites, including magnetometers and electron detectors sensitive to a large range of energies and different pitch angles. POLAR has a long orbital period (18 hours) and hence has relatively low time coverage through the radiation belts. SAMPEX has a short orbital period ($\sim$ 90 minutes) and very good time coverage of the radiation belts, but has limited spectral information and no magnetometer [*Baker et al.*, 1993]. The HEO satellite has a single integral channel which detects electrons greater than 1.5 MeV [*Blake et al.*, 1997]. The GPS satellites (NS 24 and NS 33) have an orbit such that they are near the equator at an L-shell of $\sim$ 4.2, and can obtain reasonable spectral information [*Feldman et al.*, 1985]. At geosynchronous altitudes, the Los Alamos National Laboratory (LANL) satellites 1994-084, 1991-080, and 1990-095 provide good spectral information at near equatorial latitudes [*Reeves et al.*, 1997]. The GOES satellites, also in geosynchronous orbit, provide limited spectral information, but carry magnetometers [*Space-Systems-Loral*, 1996]. Table 1 summarizes the instrumentation of each satellite included in this study.

In keeping with the assumptions detailed in Section 2, we normalize the flux levels at each

satellite to account for the energy range and pitch angle differences. First, we normalize the geosynchronous satellites (LANL & GOES) to each other by fitting the data during the rise and fall of the fluxes after the main phase of the storm to a parabola using only the data near magnetic local noon for each satellite. Fluxes are taken at local noon to minimize temporal variations on the night-side due to substorm activity. We normalize the apex of each parabola using a multiplicative factor. This factor is the normalization factor for the geosynchronous satellites. Normalization factors are less than 2 for each of the five geosynchronous satellites.

We standardize the magnetic coordinates for each satellite to a single magnetic field model. We use the Olson-Pfitzer model [*Olson and Pfitzer*, 1977] for simplicity and calculate the magnetic coordinates of each satellite. Assuming isotropic pitch angle distributions, we map the electron fluxes to the equatorial plane using a simple B_{sat}/B_{eq} multiplicative factor where B_{eq} is the equatorial magnetic field and B_{sat} is the magnetic field at the satellite.

We tie the non-geosynchronous satellite fluxes to the flux measured by POLAR at $L = 4.5 \pm 0.25$ because POLAR has a well calibrated electron detector (CEPPAD). This adjustment is done by dividing the storm period into individual 24-hour periods. The average flux at $L = 4.5 \pm 0.25$ for each satellite is then compared to the average POLAR flux for the n^{th} period and a multiplicative factor (β_n) is obtained. The mean β for each satellite is then the normalization factor for each storm at all L-shells. This factor incorporates differences in energy ranges, pitch angle coverage and background levels.

No attempt to match the geosynchronous fluxes to the POLAR fluxes is made at $L = 6.6$ because the POLAR count rates are too low at this distance to be trustworthy. However, the synthesis plots in Plate 1 show that the geosynchronous satellite fluxes match very well to the normalized fluxes at nearby L-shells.

These normalizations are necessary for producing the synthesis plots in Plates 2 and 3, but have not been applied to the data from which Plates 4, 5 or 6 were produced. When the synthesis normalizations are not applied, the nominal calibration factors for each satellite have been applied independently.

References

Abel, B., and R. M. Thorne, Electron scattering in Earth's inner magnetosphere: 1. Dominant physical processes, *J. Geophys. Res.*, *103*, 2385–2396, 1998a.

Abel, B., and R. M. Thorne, Electron scattering in Earth's inner magnetosphere: 2. Sensitivity to model parameters, *J. Geophys. Res.*, *103*, 2397–2407, 1998b.

Baker, D. N., G. M. Mason, O. Figueroa, G. Colon, J. Watzin, and R. M. Aleman, An overview of the solar, anomalous, and magnetospheric particle explorer (SAMPEX) mission, *IEEE Transactions on Geoscience and Remote Sensing*, *31*, 531–541, 1993.

Baker, D. N., et al., A strong CME-related magnetic cloud interaction with the Earth's magnetosphere: ISTP observations of rapid relativistic electron acceleration on may 15, 1997, *Geophys. Res. Lett.*, *25*, 2975–2978, 1998.

Blake, et al., CEPPAD: Comprehensive energetic particle and pitch angle distribution experiment on POLAR, *Space Sci. Rev*, *71*, 531–562, 1995.

Blake, J. B., D. N. Baker, N. Turner, K. W. Ogilvie, and R. P. Lepping, Correlation of changes in the outer-zone relativistic-electron population with upstream solar wind and magnetic field measurements, *Geophys. Res. Let.*, *24*, 927–929, 1997.

Bourdarie, S., D. Boscher, T.Beutier, J.-A. Sauvaud, and M. Blanc, Electron and proton radiation belt dynamic simulations during storm periods: A new asymmetric convection-diffusion model, *J. Geophys. Res.*, *102*, 17,541–17,552, 1997.

Brautigam, D. H., and J. M. Albert, Radial diffusion analysis of outer radiation belt electrons during the October 9, 1990, magnetic storm, *J. Geophys. Res.*, *105*, 291–309, 2000.

Elkington, S. R., M. K. Hudson, and A. A. Chan, Acceleration of relativistic electrons via

drift-resonant interaction with toroidal-mode Pc-5 ULF oscillation, *Geophys. Res. Let.*, *26*, 3273–3276, 1999.

Feldman, W., W. Aiello, D. Drake, and M. Herrin, The BDD II: An improved electron dosimeter for the global positioning system, *Tech. Rep. LA-10453-MS*, Los Alamos National Laboratory, Los Alamos, NM 87545, USA, 1985.

Friedel, R. H. W., and A. Korth, Review of CRRES ring current observations, *Adv. Sp. Res.*, *20*, 311–320, 1997.

Friedel, R. H. W., et al., A multi-spacecraft synthesis of relativistic electrons in the inner magnetosphere using LANL, GOES, GPS, SAMPEX, HEO and POLAR, *Rad. Meas. Jour.*, *18*, 589–597, 1999.

Fujimoto, M., and A. Nishida, Energization and anisotropization of energetic electrons in the Earth's radiation belt by the recirculation process, *J. Geophys. Res.*, *95*, 4265–4270, 1990.

Gonzalez, W. D., J. A. Joselyn, Y. Kamide, H. W. Kroehl, G. Rostoker, B. T. Tsurutani, and V. M. Vasyliunas, What is a geomagnetic storm?, *J. Geophys. Res.*, *99*, 5771–5792, 1994.

Green, J. C., M. G. Kivelson, and J. B. Blake, Adiabatic electron acceleration and transport during the May 15, 1997 storm, *EOS Trans. AGU*, *80*, F894, 1999.

Hudson, M. K., S. R. Elkington, J. G. Lyon, C. C. Goodrich, and T. J. Rosenberg, Simulation of radiation belt dynamics driven by solar wind variations, in *Sun-Earth Plasma Connections*, edited by J. L. Burch, R. L. Carovillano, and S. K. Antiochos, pp. 3273–3276, American Geophysical Union, Washington, D.C., USA, 1999.

Lepping, R. P., et al., The WIND magnetic-field investigation, *Space Sci. Rev*, *71*, 207–229, 1995.

Li, X. L., M. Temerin, S. Monk, and D. N. Baker, Outer belt electron enhancements by solar-wind-driven radial diffusion, *EOS Trans. AGU*, *80*, F894, 1999.

Li, X. L., et al., Energetic electron injections into the inner magnetosphere during the January 10–11, 1997 magnetic storm, *Geophys. Res. Lett.*, *25*, 2561–2564, 1998.

Liu, W. W., G. Rostoker, and D. Baker, Internal acceleration of relativistic electrons by large-amplitude ULF pulsations, *J. Geophys. Res.*, *104*, 17,391–17,407, 1999.

McIlwain, C. E., Coordinates for mapping the distribution of magnetically trapped particles, *J. Geophys. Res.*, *66*, 3681, 1966.

Meier, M. M., R. D. Belian, T. E. Cayton, R. A. Christensen, B. Garcia, K. M. Grace, J. C. Ingraham, J. G. Laros, and G. D. Reeves, The energy spectrometer for particles (ESP): Instrument description and orbital performance, in *Workshop on the Earth's Trapped Particle Environment*, edited by G. D. Reeves, vol. 383, pp. 203–210, AIP Conference Proceedings, American Institute of Physics, Woodbury, New York, 1996.

Nishida, A., Outward diffusion of energetic particles from the Jovian radiation belt, *Geophys. Res. Let.*, *81*, 1771, 1976.

Ogilvie, K. W., et al., SWE, a comprehensive plasma instrument for the wind spacecraft, *Space Sci. Rev*, *71*, 55–77, 1995.

Olson, W., and K. Pfitzer, Magnetospheric magnetic field modeling, *Annual Scientific Report, AFOSR Contract F44620-75-C-0033, McDonnell Douglas Astronaut. Co., Huntington Beach, Calif.*, 1977.

Paulikas, G. A., and J. B. Blake, Effects of the solar wind on magnetospheric dynamics: Energetic electrons at the synchronous orbit, in *Quantitative Modeling of the Magnetospheric Processes*, edited by W. Olson, pp. 180–202, American Geophysical Union, Washingto D.C., USA, 1979.

Reeves, G. D., R. D. Belian, T. C. Cayton, M. G. Henderson, R. A. Christensen, P. S. McLachlan, and J. C. Ingraham, Using Los Alamos geosynchronous energetic particle data in support of other missions, in *Satellite-Ground Based Coordination Source Book*, edited by M. Lockwood, H. J. Opgenoorth, M. N. Wild, and R. Stampe, pp. 263–272, 1997.

Reeves, G. D., R. Friedel, M. Henderson, D. Belian, M. Meier, D. Baker, T. Onsager, and H. Singer, The relativistic electron response at geosynchronous orbit during the January 1997 magnetic storm, *J. Geophys. Res.*, *103*, 17,559–17,570, 1998a.

Reeves, G. D., R. H. W. Friedel, and R. Hayes, Maps could provide space weather forecasts for the inner magnetosphere, *EOS Trans. AGU*, *79*, 613–618, 1998b.

Reeves, G. D., et al., The global response of relativistic radiation belt electrons to the January 1997 magnetic cloud, *Geophys. Res. Lett.*, *25*, 3265–3268, 1998c.

Roederer, J. G., *Dynamics of Geomagnetically Trapped Radiation*, Springer, New York, 1970.

Schulz, M., and L. J. Lanzerotti, *Particle Diffusion in the Radiation Belts*, 1st ed., Springer Co., New York, 1973.

Selesnick, R. S., and J. B. Blake, On the source location of radation belt relativistic electrons, *J. Geophys. Res.*, *105*, 2607–2624, 2000.

Space-Systems-Loral (Ed.), *GOES I-M Databook, Revison 1*, chap. Space Environment Monitor Subsystem, pp. 58–66, Space Systems-Loral, 1996.

West, H. I., R. M. Buck, and J. R. Walton, Electron pitch angle distributions throughout the magnetosphere as observed by OGO 5, *J. Geophys. Res.*, *78*, 1064–1081, 1973.

K. L. McAdams, G. D. Reeves, R. H. W. Friedel and T. E. Cayton, Los Alamos National Laboratory, P.O. Box 1663, MS D466, Los Alamos, NM 87545 (email: kmcadams00@earthlink.net, reeves@lanl.gov, rfriedel@lanl.gov, and tcayton@lanl.gov)

Received _____

To be published in *Journal of Geophysical Research*, 2000. 1st revision, September 25, 2000

This manuscript was prepared with AGU's LaTeX macros v5, with the extension package 'AGU^{++}' by P. W. Daly, version 1.6b from 1999/08/19.

Figure Captions

Figure 1. Solar wind conditions for the four storms: a) January 97; b) May 97; c) September 98; and d) October 98. The top panel in each stack shows the Dst index (nT) and the second panel in each stack shows the Kp index. The lower three panels and show the z-component of the interplanetary magnetic field (B_z), the solar wind ion density (n_{sw}, cm^3), and the solar wind velocity (v_{sw}) in km/s, respectively.

Plate 1. Global relativistic electron fluxes (E > 1.5 MeV) as a function of time and L-shell. Data from eleven satellites have been combined, as described in the text, to provide higher spatial and temporal coverage than is available from any single satellite. The four GEM storms, a) January 97, b) May 97, c) September 97, d) October 98, each show unique features associated with the different solar wind driving conditions.

Plate 2. Relativistic electron fluxes (E > 1.5 MeV) from ten satellites at $L = 4.25 \pm 0.125$ (top) and $L = 6.6 \pm 0.125$ (bottom) for a) January 97, b) May 97, c) September 97, and d) October 98. The fluxes from each satellite are plotted in a different color. The distinctly different temporal behavior of the fluxes at fixed energy at $L \sim 4.2$ and $L \sim 6.6$ seen by *Reeves et al.* [1998c] for the January 97 storm are a consistent feature of these four events.

Plate 3. Spectral evolution of the relativistic electron fluxes for the four GEM storms at $L = 4.25 \pm 0.125$ (GPS, red) and $L = 6.6 \pm 0.125$ (LANL, blues). C and E_o are the coefficients of the spectral fit to a power law: $f(E) = C \exp(-E/E_o)$. These spectral fit parameters show a more consistent behavior than do the fluxes at fixed energies. All four storms show a rapid decrease in C at both $L \sim 4.2$ and $L \sim 6.6$ following storm onset and an increase in the spectral hardness, E_o, which is much more dramatic at $L \sim 4.2$ than at $L \sim 6.6$.

Plate 4. Phase space density ($cm^{-2}s^{-1}MeV^{-2}$) at constant μ at $L = 4.25 \pm 0.125$ (GPS, red) and $L = 6.6 \pm 0.125$ (LANL, blues) for different values of μ (in MeV/G). In each stack, panels show the phase space density for the two L-shells at increasing values of μ for, a) January 97 and b) May 97. For all four storms the gradient in phase space density is larger at smaller μ. At lower values of μ the phase space density decreases with time and the gradient remains nearly constant. At higher values of μ the phase space density increases or remains nearly constant. The increase is more rapid at $L \sim 4.2$ so the gradient decreases with time.

Plate 5. Similar to Plate 4 except for a) September 98 and b) October 98

Tables

Table 1. Satellite Specification

Satellite	Energy range (electrons, MeV)	Magnetometer	Apogee ($\sim R_e$)	Period (hours)
POLAR	$E > 1.4$	yes	9.1	18
GOES (8 & 9)	$E > 2$	yes	6.6	24
GPS (24 & 33)	$E > 1.6$	no	4.0	12
LANL (084, 080, 095)	$E > 1.8$	no	6.6	24
HEO	$E > 1.5$	no	7.2	12
SAMPEX	$2 < E < 6$	no	1.1	1.5

Table 2. Overview of GEM storms

	January 97	May 97	September 98	October 98
Dst Minimum (nT)	-78	-115	-233	-139
Kp Maximum	6	6^+	8^-	6^+
Density (SW) (cm^{-3})	200	44	22	68
Wind Velocity (SW) (km/s)	575	524	901	693
Ion pressure (SW) (nPa)	53	17	24	25
Peak Flux at $L = 4.4$	1×10^5	2×10^5	4×10^5	3×10^5
Peak Flux at L=6.6	3×10^3	3×10^3	7×10^3	2×10^4
Polar Cap Index	NA	40	100	45

Figures

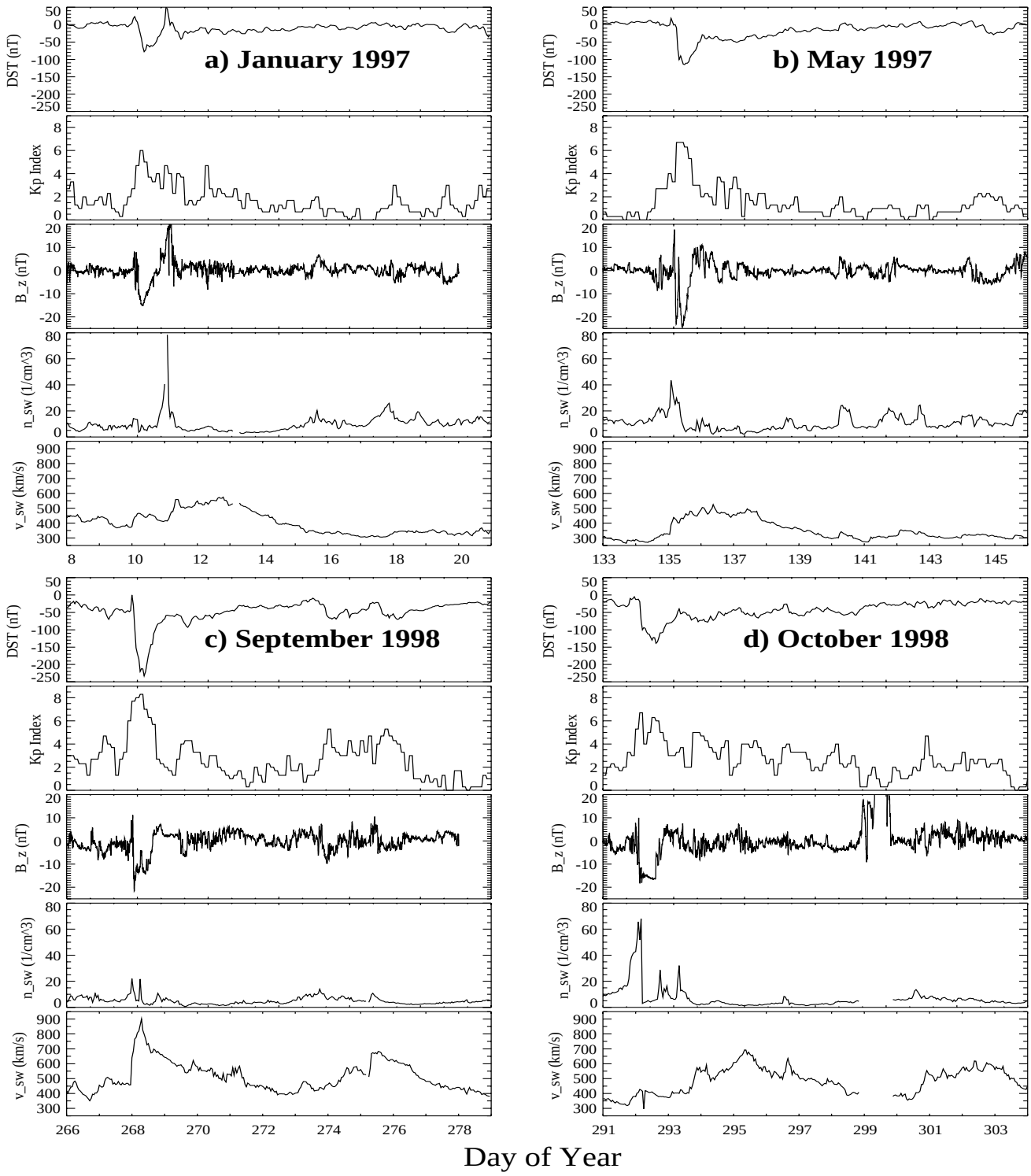

Figure 1. Solar wind conditions for the four storms: a) January 97; b) May 97; c) September 98; and d) October 98. The top panel in each stack shows the Dst index (nT) and the second panel in each stack shows the Kp index. The lower three panels and show the z-component of the interplanetary magnetic field (B_z), the solar wind ion density (n_{sw}, cm^3), and the solar wind

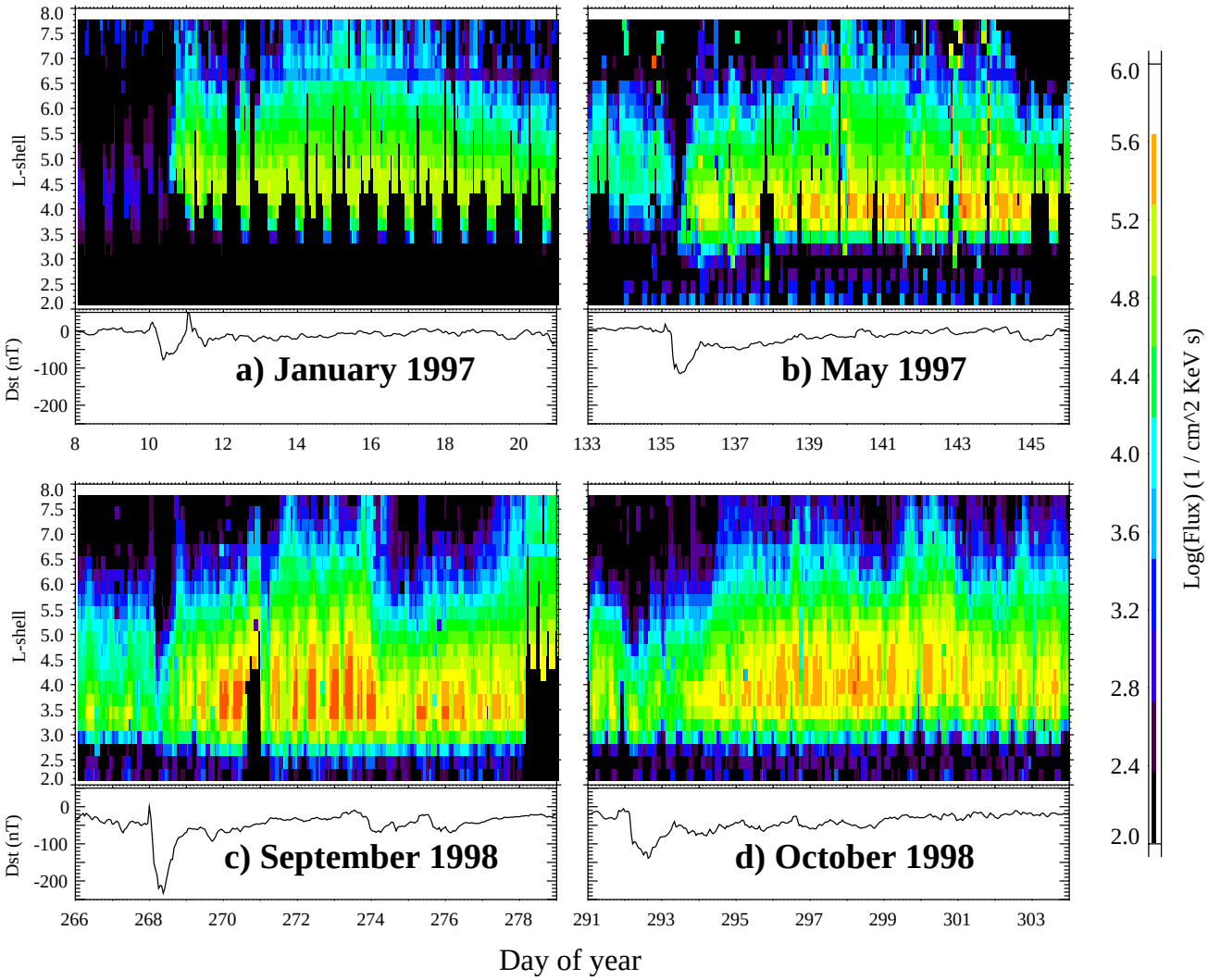

Plate 1. Global relativistic electron fluxes (E > 1.5 MeV) as a function of time and L-shell. Data from eleven satellites have been combined, as described in the text, to provide higher spatial and temporal coverage than is available from any single satellite. The four GEM storms, a) January 97, b) May 97, c) September 97, d) October 98, each show unique features associated with the different solar wind driving conditions.

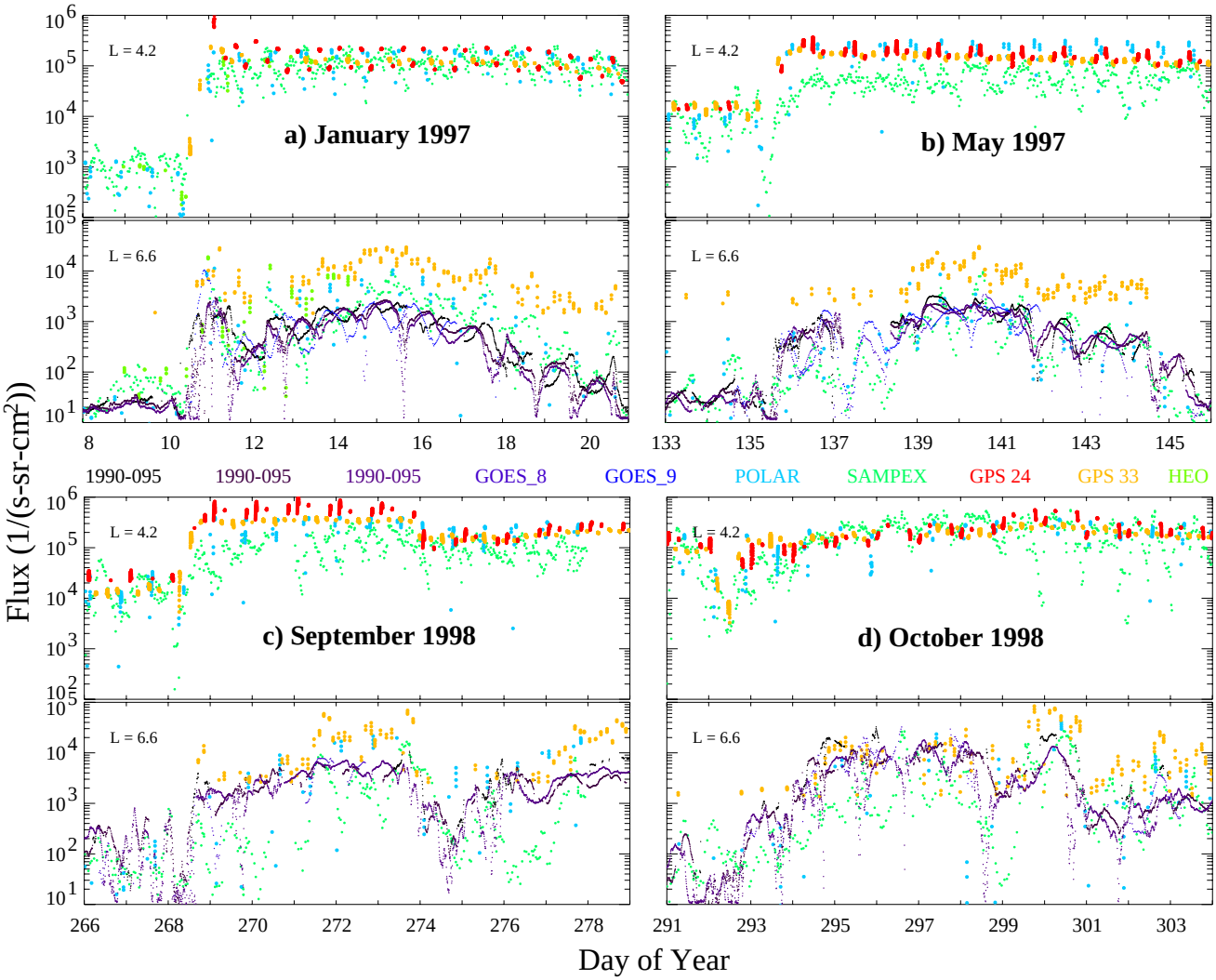

Plate 2. Relativistic electron fluxes (E > 1.5 MeV) from ten satellites at $L = 4.25 \pm 0.125$ (top) and $L = 6.6 \pm 0.125$ (bottom) for a) January 97, b) May 97, c) September 97, and d) October 98. The fluxes from each satellite are plotted in a different color. The distinctly different temporal behavior of the fluxes at fixed energy at $L \sim 4.2$ and $L \sim 6.6$ seen by *Reeves et al.* [1998c] for the January 97 storm are a consistent feature of these four events.

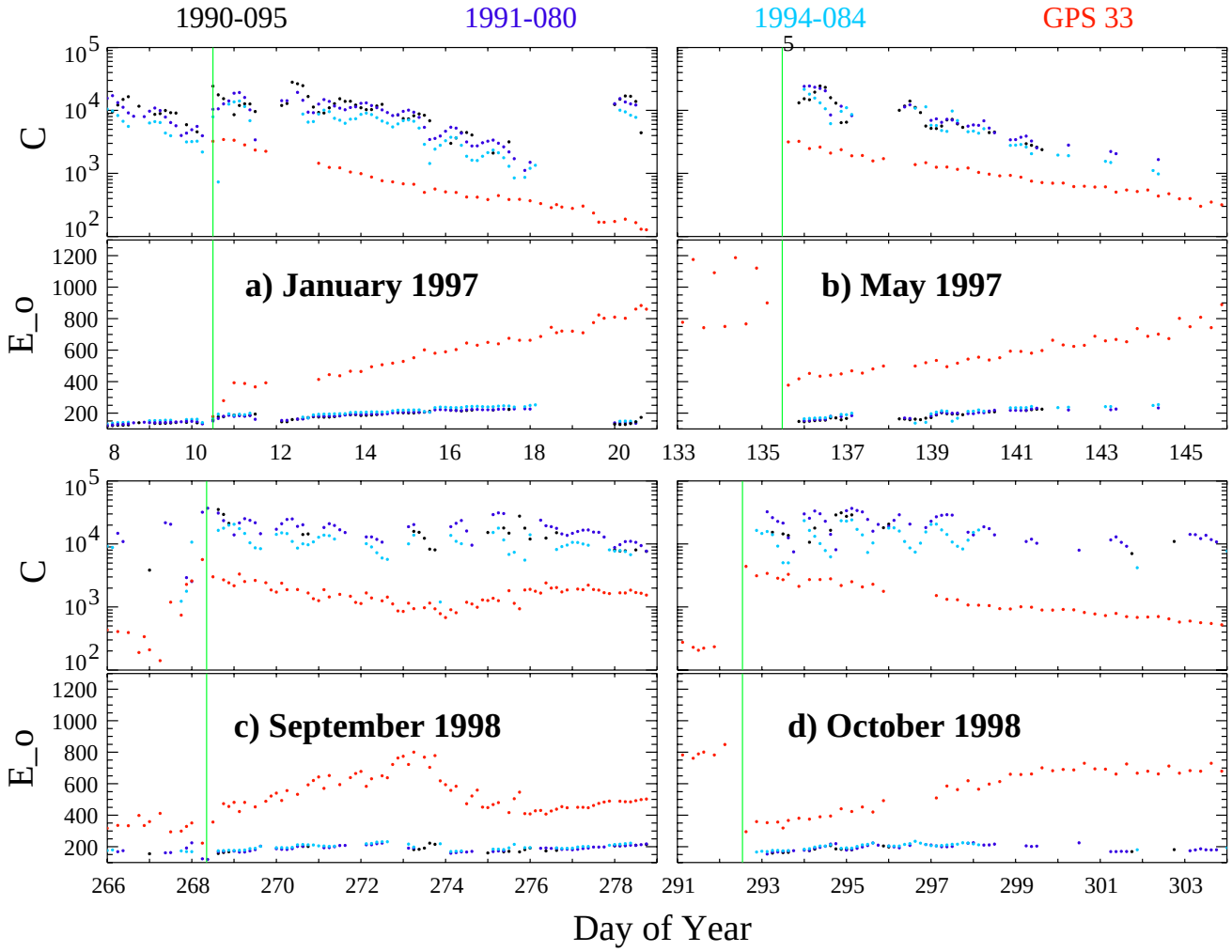

Plate 3. Spectral evolution of the relativistic electron fluxes for the four GEM storms at $L = 4.25 \pm 0.125$ (GPS, red) and $L = 6.6 \pm 0.125$ (LANL, blues). C and E_o are the coefficients of the spectral fit to a power law: $f(E) = C \exp(-E/E_o)$. These spectral fit parameters show a more consistent behavior than do the fluxes at fixed energies. All four storms show a rapid decrease in C at both $L \sim 4.2$ and $L \sim 6.6$ following storm onset and an increase in the spectral hardness, E_o, which is much more dramatic at $L \sim 4.2$ than at $L \sim 6.6$.

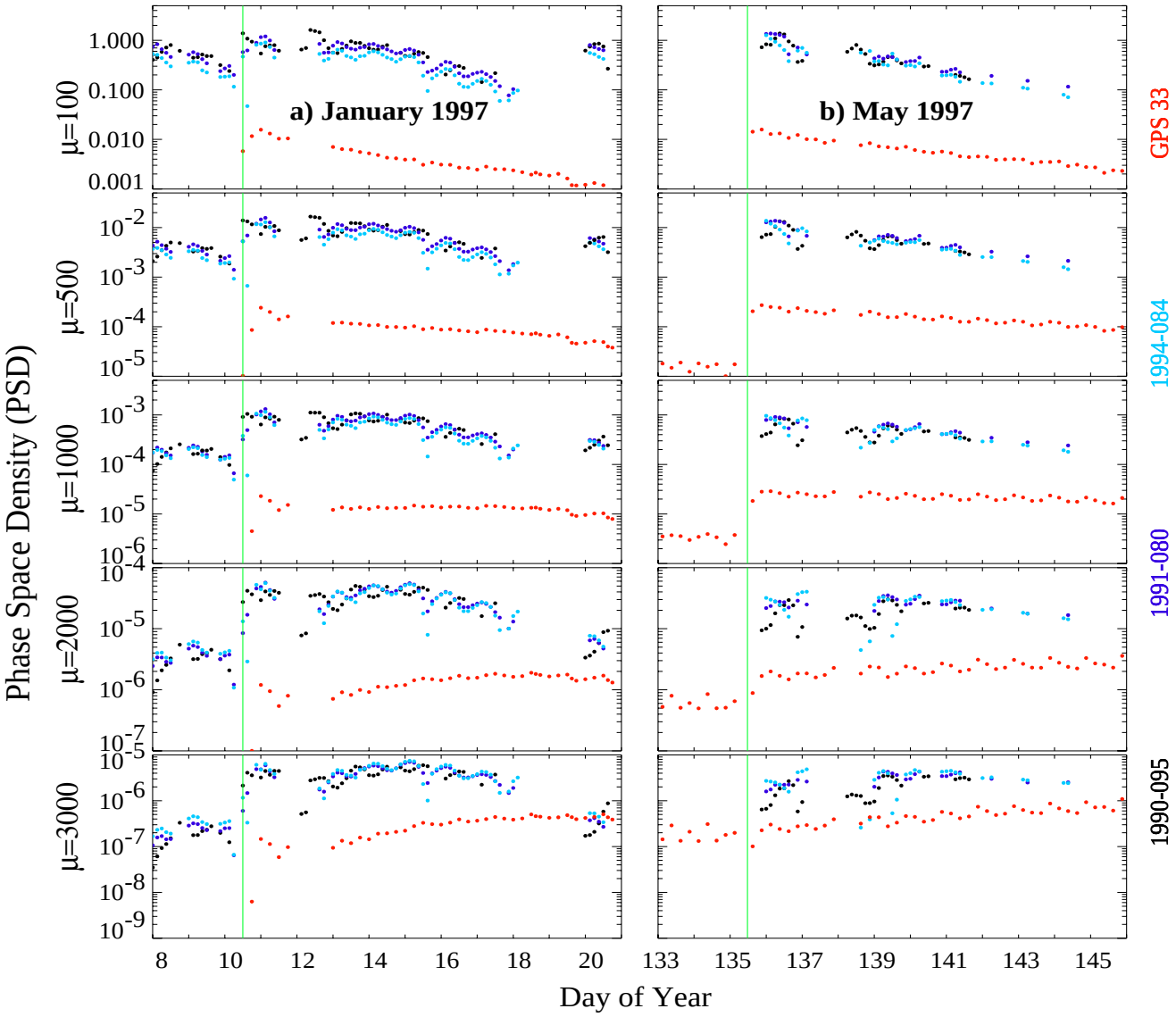

Plate 4. Phase space density ($cm^{-2}s^{-1}MeV^{-2}$) at constant μ at $L = 4.25 \pm 0.125$ (GPS, red) and $L = 6.6 \pm 0.125$ (LANL, blues) for different values of μ (in MeV/G). In each stack, panels show the phase space density for the two L-shells at increasing values of μ for, a) January 97 and b) May 97. For all four storms the gradient in phase space density is larger at smaller μ. At lower values of μ the phase space density decreases with time and the gradient remains nearly constant. At higher values of μ the phase space density increases or remains nearly constant. The increase is more rapid at $L \sim 4.2$ so the gradient decreases with time.

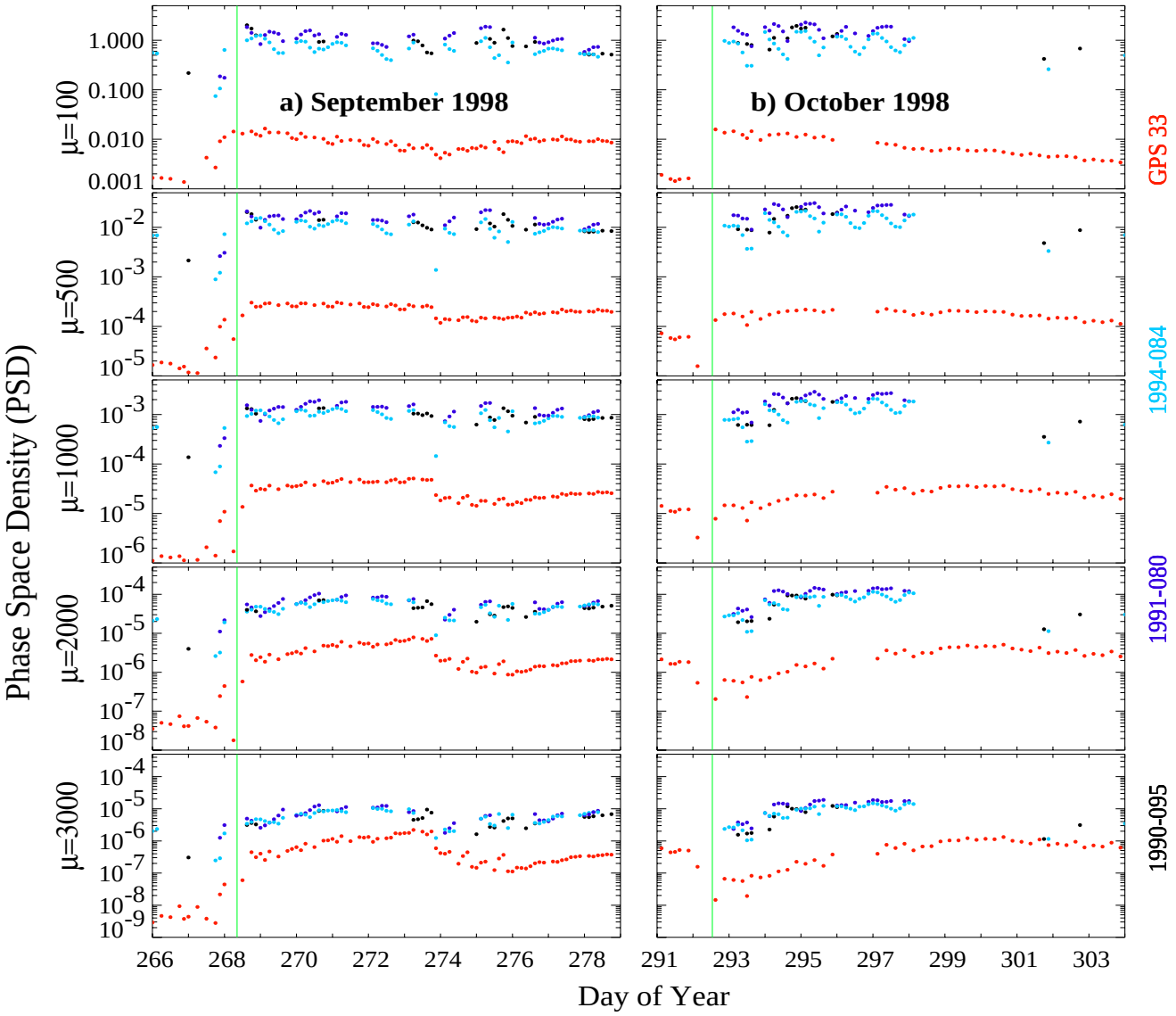

Plate 5. Similar to Plate 4 except for a) September 98 and b) October 98